Differential anomalous scattering on Fe-Co-based metallic glasses

1999 J. Phys.: Condens. Matter 11 10199

(http://iopscience.iop.org/0953-8984/11/50/312)

J. Phys.: Condens. Matter **11** (1999) 10199–10210. Printed in the UK PII: S0953-8984(99)98595-8

Differential anomalous scattering on Fe–Co-based metallic glasses

C Meneghini†‡, A Balerna‡, S Mobilio‡§, M L Fdez-Gubieda‖, I Orue¶ and A García-Arribas‖

† Istituto Nazionale di Fisica della Materia c/o GILDA–ESRF Grenoble, France
‡ Laboratori Nazionali di Frascati (INFN), PO Box 13, I-00044 Frascati, Italy
§ Dipartimento di Física 'E Amaldi', Universitá di Roma Tre, Via della Vasca Navale 84, I-00146 Roma, Italy
‖ Departamento de Electricidad y Electrónica, Facultad de Ciencias, Universidad del País Vasco, Apartado 644, 48080 Bilbao, Spain
¶ Departamento de Física, Facultad de Ciencias, Universidad de Oviedo, Avenida Calvo Sotelo, s/n 33007 Oviedo, Spain

E-mail: cmeneghi@lnf.infn.it

Received 22 October 1998, in final form 13 July 1999

Abstract. Fe–Co-based amorphous alloys were studied by x-ray diffraction and anomalous x-ray diffraction methods for a range of sample compositions and preparation methods. The main structural characteristics at short- and medium-range scales were investigated. The presence of chemical ordering with preferred Co–Co and Fe–Fe homonuclear correlations and partial Fe-rich phase separation, suggested from previous extended x-ray absorption fine-structure experiments, were clearly in evidence.

1. Introduction

The local atomic structure of Fe–Co-based amorphous alloys is a subject of great interest since it has a large influence on the interesting and unique properties (mechanical, magnetic, etc) of these materials [1]. On the other hand, from a fundamental point of view, obtaining detailed knowledge of the local structure at short- and medium-range scales for these materials represents an interesting problem related to the physics of disordered systems.

In an amorphous system, due to the lack of translational symmetry, it is especially difficult to determine the local structure. In this point resides the importance of experimental probes sensitive to the local arrangement of the atoms. Besides, more valuable information is obtained when the technique is element sensitive, that is, capable of determining the atomic configuration around a given type of atom. This is the case for the techniques of EXAFS (extended x-ray absorption fine structure) and DAS (differential anomalous scattering).

In any case, to obtain information from the measured data, it is necessary to use a structural model. The simplest scheme used for describing the structure of the amorphous alloys is the model of dense random packing of hard spheres (DRPHS) [2, 3], which assumes the atoms to be rigid spheres packed in a cluster, dense because it does not contain voids large enough to accommodate another sphere, and random because it lacks long-range order. This simple model has been widely and successfully used to interpret the data from x-ray diffraction and EXAFS studies [4–7].

0953-8984/99/5010199+12$30.00

In multicomponent alloys, this simple model can be extended to account for specific chemical affinities between different elements. Such chemical short-range order lies behind the simple and well establish conclusion that two metalloids avoid direct contact and are exclusively bound to metal atoms. In fact, previous work on the short-range order of (FeCo)SiB amorphous alloys by means of EXAFS and XANES (x-ray near edge structure) spectroscopies [7, 8] proved the existence of a chemical short-range order with a preferential coordination of Si atoms with Co and B atoms with Fe. In the Co-rich alloys this chemical affinity induces a highly ordered structure around the Fe species. This ordered structure is an intrinsic property of the Co-rich alloys, does not depend on the sample preparation and appears only when the Si or P content is higher than the Fe content [9]. The lack of variation of the Co environment in these compounds suggests that the Fe atoms form a well defined structural unit randomly distributed in a uniform Co amorphous matrix.

Such an ordered Fe-rich phase has been suggested to be the precursor of an Fe bcc phase developed in the first stages of the crystallization process of CoSiBM (M = Nb, Cr) amorphous alloys, when a small amount of Fe enters the composition [10].

EXAFS spectroscopy is a local probe that can be used to accurately determine the local short-range order, but it is not sensitive to medium- and long-range order and cannot be used to reveal the topological order induced by these chemical affinities. The use of a complementary technique such as x-ray scattering (XRS) or differential anomalous scattering (DAS) gives more insight into the atomic structure of these materials. As explained in more detail in section 2, combining the XRS and DAS techniques it is possible to probe medium- and long-range atomic correlations, with the possibility of partially distinguishing between the contributions of the different species in the sample. In this paper we use the XRS and DAS techniques to investigate the structure of complex amorphous samples of $(Fe_xCo_{1-x})_{0.75}Si_{0.15}B_{0.1}$ ($x = 0.2$, 0.06) and $(Fe_{0.08}Co_{0.92})_{0.83}P_{0.17}$ in order to supplement the information obtained in previous EXAFS work [9] with the inclusion of medium-range-order features, and to unambiguously demonstrate the existence of a chemical ordering. The existence or non-existence of ordered structures in the precursor glass is in fact a crucial point in the study of the crystallization processes for the new Co-rich nanocrystals [10–12]

The paper is organized in the following way: section 2 deals with the formalism of anomalous x-ray scattering; sections 3 and 4 concern the experimental procedure and data analysis; section 5 presents the results and discussion; and finally, section 6 summarizes the main conclusions.

2. X-ray scattering and the anomalous x-ray scattering formalism

The total structure factor $S(q)$ contains all of the structural information from wide-angle x-ray scattering (XRS) experiments [13]. In multicomponent materials composed of n atomic species, according to the Faber–Ziman formalism, $S(q)$ can be written as a weighted sum of $n(n+1)/2$ partial structure factors $s_{\alpha\beta}(q)$:

$$S(q) = \sum_{\alpha \geqslant \beta} w_{\alpha\beta}(q, E) s_{\alpha\beta}(q) \tag{1}$$

with

$$w_{\alpha\beta}(q, E) = \frac{x_\alpha x_\beta f_\alpha^*(q, E) f_\beta(q, E)}{|\langle f(q, E)\rangle|^2} \qquad |\langle f(q, E)\rangle|^2 = \left| \sum_\alpha x_\alpha f_\alpha \right|^2 . \tag{2}$$

Here x_α is the atomic fraction of the species α and f_α is the atomic scattering amplitude, given by

$$f_\alpha(q, E) = f_\alpha^0(q) + f_\alpha'(E) + \mathrm{i} f_\alpha''(E) \tag{3}$$

where $f_\alpha^0(q)$ is the energy-independent Thompson scattering factor and $f_\alpha'(E)$ and $f_\alpha''(E)$ are the real and imaginary parts of the dispersion corrections. These dispersion corrections change abruptly when the x-ray energy is tuned near an absorption edge of the species α [14]; on the other hand their q-dependence is negligible.

Each $s_{\alpha\beta}(q)$ is related to the partial pair correlation function $g_{\alpha\beta}(r)$ by a Fourier transform (FT):

$$g_{\alpha\beta}(r) = 1 + \frac{1}{2\pi^2 r\rho} \int q(s_{\alpha\beta}(q) - 1) \sin(qr)\, \mathrm{d}q \tag{4}$$

in which ρ is the average atomic number density (atoms Å^{-3}). In analogy to (4) the total pair correlation function, $g(r)$, can be calculated from the experimental $S(q)$ [13]:

$$g(r) = 1 + \frac{1}{2\pi^2 r\rho} \int q(S(q) - 1) \sin(qr)\, \mathrm{d}q. \tag{5}$$

$g(r)$ is then the sum of convolution products of each $g_{\alpha\beta}$ and $M_{\alpha\beta}$: $\sum_{\alpha\beta} M_{\alpha\beta} \otimes g_{\alpha\beta}$, where $M_{\alpha\beta}$ is the FT of the weighting functions $w_{\alpha\beta}$ times the window function representing the q-space extent of the experimental data. Dealing with materials composed of many atomic species, a single diffraction experiment cannot yield the individual partial pair correlation functions, since it is their weighted sum that contributes to $S(q)$. In principle, having $n(n+1)/2$ independent $S(q)$ measurements, it could be possible to determine all the $s_{\alpha\beta}(q)$ ($g_{\alpha\beta}(r)$) [15]. In practice this can be done only for binary systems, using neutron scattering with isotopic substitution and/or the anomalous x-ray scattering (AXS) technique.

Differential anomalous scattering (DAS) [16] represents a particular approach to the AXS techniques which allows one to select structural information relative to the surrounding of a particular atomic species in the sample. Given two XRS data sets measured at energies near to (E_1) and far from (E_2) the absorption edge of the atomic species A, the differential structure factor $\Delta S_A(q)$ for the species A is calculated as

$$\Delta S_A(q, E_1, E_2) = \frac{S(q, E_1)\,|\langle f(q, E_1)\rangle|^2 - S(q, E_2)\,|\langle f(q, E_2)\rangle|^2}{|\langle f(q, E_1)\rangle|^2 - |\langle f(q, E_2)\rangle|^2} \tag{6}$$

where $S(q, E)$ is the total structure factor measured at the photon energy E. In a first approximation, i.e. neglecting the differences in the dispersion corrections of the atomic species different from A, it turns out that

$$\Delta S_A(q, E_1, E_2) \simeq \sum_\beta \Delta w_{A\beta}(q, E_1, E_2) s_{A\beta}(q) \tag{7}$$

in which

$$\Delta w_{A\beta}(q, E_1, E_2) = \frac{w_{A\beta}(q, E_1)\,|\langle f(q, E_1)\rangle|^2 - w_{A\beta}(q, E_2)\,|\langle f(q, E_2)\rangle|^2}{|\langle f(q, E_1)\rangle|^2 - |\langle f(q, E_2)\rangle|^2}. \tag{8}$$

From $\Delta S_A(q)$ (the differential correlation function), $\Delta g_A(q)$ is defined in analogy to (4). In this approximation, the sum in (7) runs only over β, meaning that only the correlations between atom A and all of the other atomic species β contribute to $\Delta S_A(q)$ and $\Delta g_A(q)$. This approximation fails when also the dispersion corrections of the other species vary appreciably between the two data sets. In that case the other partial terms that contribute to ΔS_A must also be considered.

It is worth noting that the structural information contained in ΔS_A resembles that obtainable from EXAFS measurements, as both describe the local structure around specific atomic species. However, XRS and DAS are largely complementary to EXAFS: the extension of scattering data to low q-values allows the investigation of the medium- and long-range structure, while EXAFS is sensitive mainly to the nearest-neighbour distributions. The combination of these techniques permits a detailed knowledge of the sample structure to be obtained.

3. Experimental procedures

Two amorphous samples of composition $(Fe_xCo_{1-x})_{0.75}Si_{0.15}B_{0.1}$ with $x = 0.2$ and 0.06, that will be indicated as **Fe20** and **Fe6** in the following, were prepared by the standard single-roller quenching (SRQ) technique in the form of long ribbons 0.5 mm wide and 20 μm thick. Another sample, of composition $(Fe_xCo_{1-x})_{0.83}P_{0.17}$ ($x = 0.08$; sample **Fe8**) was prepared by electrodeposition (ED) [17] in the form of a film with a thickness of 10 μm.

XRS measurements were carried out at the GILDA (General Italian Line for Diffraction and Absorption) beamline [18, 19] of the European Synchrotron Radiation Facility (ESRF) at different energies (22 keV, 10 keV and 7.709 keV (Co K edge)). The beam energies were defined using a Si(311) double-crystal monochromator working in the sagittal focusing mode which concentrates about 4 mrad of horizontal-source divergence in a small (3×1 mm^2) and intense (10^9 photons s^{-1} at 7.709 keV and 10^{10} photons s^{-1} at 22 keV) focal spot on the sample. Two Pd-coated, grazing-incidence mirrors focus the beam vertically and ensure a harmonic-free beam at the energies used (the cut-off energy is 23–24 keV). For data normalization, the incident intensity is detected by an air-filled ionization chamber. Samples were mounted on the horizontal axis of a two-circle diffractometer. The intensities of the scattered x-ray were first filtered using a Ge(220) crystal analyser (CA) and then detected by a NaI(Tl) scintillation counter. The main advantage of such a configuration, as compared to the use of solid-state detectors, is that the CA acts as a band-pass filter selecting a small energy window around the elastic peak, cutting off most of the inelastic contributions such as the fluorescence (particularly inconvenient when measuring XRS spectra near an absorption edge) and some of the Compton scattering (in particular at high angles). In this way, low-noise data are obtained. Moreover, the rejection of Kβ fluorescence makes possible to measure the XRS exactly at the edge energies where f' takes its minimum, maximizing the resonance effect. Using solid-state detectors, Kβ fluorescence is not resolved from the elastic peaks; therefore working energies are normally chosen somewhat lower than the edge energy to reduce the background.

The energy resolution of the crystal analyser is given by [20]:

$$\Delta E/E \sim (h/L)\cot g(\theta_b) \tag{9}$$

where h is the vertical beam size, $L = 220$ mm is the distance between the sample and the analyser and θ_b is the Bragg angle of the crystal. A beam size of $h = 1$ mm was chosen when working far above the Co K edge in order to maximize the flux on the scintillator (lower energy resolution, wider angular acceptance). However, when working at the Co K edge, the vertical beam size selected was $h = 0.5$ mm (giving $\Delta E/E \simeq 0.005$) which makes it possible to resolve both Kα and Kβ fluorescence from the elastic peak. Cutting off all of the fluorescence simplifies the data reduction. On the other hand, the small angular acceptance of the CA represents the principal handicap when studying amorphous samples, since these materials present weak and little-structured XRS signals.

The measurements performed are summarized in table 1. To identify them, we have added a letter to the sample name: **a** indicates the XRS data recorded far above the Co K edge (at

Table 1. Energies used for XRS and DAS data.

Sample	Composition	Energy (keV)
Fe20a	$(Fe_{0.2}Co_{0.8})_{0.75}Si_{0.15}B_{0.1}$	22.000
Fe6a	$(Fe_{0.06}Co_{0.94})_{0.75}Si_{0.15}B_{0.1}$	22.000
Fe6b	$(Fe_{0.06}Co_{0.94})_{0.75}Si_{0.15}B_{0.1}$	7.709
Fe6Δ	$(Fe_{0.06}Co_{0.94})_{0.75}Si_{0.15}B_{0.1}$	22.000 and 7.709
Fe8a	$(Fe_{0.08}Co_{0.92})_{0.87}P_{0.13}$	10.000
Fe8b	$(Fe_{0.08}Co_{0.92})_{0.87}P_{0.13}$	7.709
Fe8Δ	$(Fe_{0.08}Co_{0.92})_{0.87}P_{0.13}$	10.000 and 7.709

22 keV for **Fe20a** and **Fe6a** and at 10 keV for **Fe8a**); **b** designates the XRS data obtained at the Co K edge: 7.709 keV (**Fe6b** and **Fe8b**); finally **Fe6Δ** (**Fe8Δ**) means DAS data calculated for sample **Fe6** (**Fe8**), from **Fe6a** (**Fe8a**) and **Fe6b** (**Fe8b**) measurements.

Anomalous scattering data were reported only for the Co K edge, since, on the one hand, the low energy of the Fe absorption edge (7.112 keV) reduces the q-range of the diffraction spectrum too much and, on the other hand, the photon flux is appreciably reduced resulting in insufficient data statistics.

Figure 1 reports the raw XRS data as functions of the exchange momentum: $q = 4\pi \sin(\theta)/\lambda$. Data were recorded at constant $\mathrm{d}q = 0.05$ Å^{-1}, in θ–2θ geometry (with θ between 3° and 65°). The melt-spun samples (**Fe6** and **Fe20**) were measured in symmetrical reflection geometry while the electrodeposited sample **Fe8** was measured in symmetrical transmission geometry. For the XRS spectra obtained at energies above the Co K edge, four scans were averaged (3 h/sample); while for those spectra measured at the energy of the Co K edge, eight scans were used in the average (9–10 h/sample).

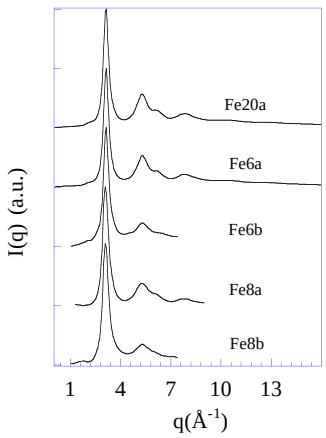

Figure 1. Raw XRS data for the samples studied.

In order to select the energy of the beam at the Co K edge, we look for the minimum of f'_{Co} situated at the maximum of the absorption coefficient derivative: $\mathrm{d}\mu(E)/\mathrm{d}(E) = 7.709$ keV. The energy calibration of the beamline was controlled at the beginning and at the end of each diffractogram. The edge position was well reproduced within 0.5 eV which demonstrates the high stability of the beamline.

4. Data analysis

XRS data were treated using standard procedures for incident intensity normalization, background subtraction (air scattering was independently measured and subtracted off), absorption and geometrical corrections [13]. The Compton scattering contribution was calculated using the tabulated [21] theoretical values, corrected for the analyser resolution window.

To calculate the weight functions $w_{\alpha,\beta}$, theoretical values were used for f_α^0 [22] and for the dispersion corrections [23]. Only at the Co K edge were Co dispersion corrections calculated from the absorption coefficient, $\mu_{\mathrm{Co}}(E)$, using the Kramers–Kronig relations [24]. We found values 10% reduced with respect to the theory, due to the experimental resolution and core-hole width (table 2). In table 3 we report the $\langle w_{\alpha\beta}\rangle/x_\beta$ and $\langle \Delta w_{\alpha\beta}\rangle/x_\beta$ values that are the weight functions (2) averaged over the experimental q-range and divided by the concentration of the species β. They give an estimation of the relative weight through which each α–β pair contributes to $S(q)$ or $\Delta S(q)$ (see equations (1), (7) and (10)). Looking at table 3, it is evident that the Co β contributions still dominate both $S(q)$ and ΔS_{Co} for all of the samples. Nevertheless, the contribution of other α–β pairs like Fe–Fe and Si–Si must be considered. In fact, they have non-negligible weight factors. Moreover the large energy difference between **Fe6a** and **Fe6b** data sets, as well as between **Fe8a** and **Fe8b** data sets, also produces large changes in the weight factors of pairs not involving the Co, like Fe–Fe. Thus, investigating

Table 2. Dispersion corrections as a function of the energies of XRS experiments as reported by Sasaki [23]. For Co at 7.709 keV the experimental values are reported and compared with the theoretical ones (reported in brackets).

Energy	Co		Fe		Si		P		B	
(keV)	f'	f''	f'	f''	f'	f''	f'	f''	f'	f''
22.0	0.26	0.63	0.24	0.55	0.042	0.043	0.041	0.058	0.0003	0.0004
10.0	−0.33	2.55	−0.075	2.24	0.256	0.362	0.218	0.286		
7.709	−10(11.4)	2.7(3.9)	−1.72	3.43	0.256	0.36	0.3	0.47	0.009	0.004

Table 3. Weight factors $\langle w_{\alpha\beta}\rangle/x_\beta$ and $\langle \Delta w_{\mathrm{Co}\beta}\rangle/x_\beta$.

	Fe20	**Fe6**			**Fe8**		
	a	**a**	**b**	**Δ**	**a**	**b**	**Δ**
α–β	$\frac{\langle w_{\alpha-\beta}\rangle}{x_\beta}$	$\frac{\langle w_{\alpha-\beta}\rangle}{x_\beta}$	$\frac{\langle w_{\alpha-\beta}\rangle}{x_\beta}$	$\frac{\langle \Delta w_{\alpha-\beta}\rangle}{x_\beta}$	$\frac{\langle w_{\alpha-\beta}\rangle}{x_\beta}$	$\frac{\langle w_{\alpha-\beta}\rangle}{x_\beta}$	$\frac{\langle \Delta w_{\alpha-\beta}\rangle}{x_\beta}$
Co–Co	0.88	1.01	0.69	1.11	0.91	0.65	1.0
Co–Fe	1.67	1.22	3.11	1.78	1.71	2.29	1.43
Co–Si	0.80	0.93	1.53	0.80			
Co–P				1.0	1.46	0.73	
Co–B	0.2	0.3	0.4	0.2			
Fe–Fe	0.2	0.13	0.2	0.013	0.11	0.29	0.01
Fe–Si	0.3	0.07	0.33	5×10^{-3}			
Fe–P				0.12	0.31	8×10^{-3}	
Fe–B	0.06	0.02	0.08	2×10^{-3}			
Si–Si	0.05	0.06	0.2	4×10^{-3}			
P–P				0.08	0.15	8×10^{-4}	
Si–B	0.02	0.02	0.1	8×10^{-4}			
B–B	2×10^{-3}	2×10^{-3}	0.02	3×10^{-5}			

this effect also gives a good opportunity to get insight into the local structure around species other than Co.

The q-weighted values $q(S(q)-1)$ and $q(\Delta S_{\mathrm{Co}}(q)-1)$ obtained from the XRS are reported in figures 2 and 3. High-energy data (**Fe20a**, **Fe6a**) have good signal-to-noise ratios up to $q = 15$ Å^{-1}. As an intrinsic effect of the exchange momentum–energy definition, the reciprocal space of the spectra recorded at low energies is reduced. Therefore, $S(q)$ for sample **Fe8a** reaches $q = 9$ Å^{-1} while the Co K-edge data and $\Delta S(q)$ are limited to $q = 7$ Å^{-1}. The high quality of the XRS data allowed us to obtain a good signal-to-noise ratio for the differential structure factors.

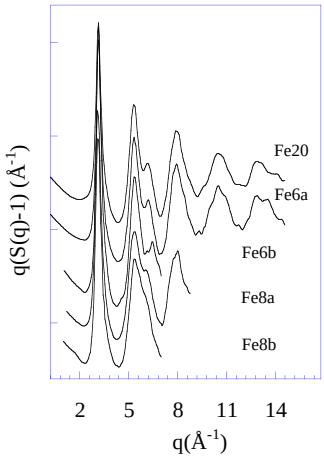

Figure 2. Total structure factors weighted by q: $q(S(q)-1)$.

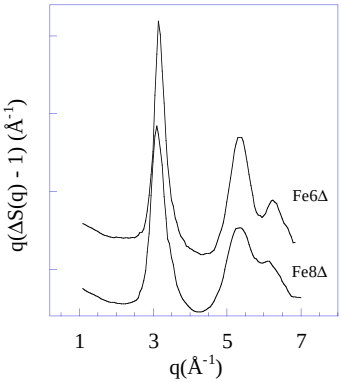

Figure 3. Differential structure factors calculated at the Co K edge and weighted by q: $q(\Delta S(q)-1)$.

Figure 4 reports all of the experimental $g(r)$ and $\Delta g_{\mathrm{Co}}(r)$ data (dots). Such data were fitted in the r-range 0–5.3 Å using a theoretical function $g^{th}(r)$ ($\Delta g^{th}(r)$) to obtain quantitative structural parameters. The $g^{th}(r)$ ($\Delta_{\mathrm{Co}} g^{th}(r)$) were calculated by building up the corresponding $S^{th}(q)$ ($\Delta S^{th}_{\mathrm{Co}}(q)$) in reciprocal space, and were in turn Fourier transformed in the same q-range of the corresponding experimental data. This method allows one to reproduce not only the true structural features of $g(r)$ and $\Delta g(r)$, but also the unphysical oscillations due to FT truncation effects, which are not negligible in the low-energy $g(r)$ or in $\Delta g(r)$ (figures 4 and 5). The fitting of the data in real space is preferred over that in reciprocal space, because in real space the structural features relative to different coordination shells can be easily individuated and separately analysed.

The $S^{th}(q)$ ($\Delta S^{th}_{\mathrm{Co}}(q)$) were calculated using the Debye equation for the partial contributions [13]:

$$s^{th}_{\alpha\beta}(q) = \frac{N_{\alpha\beta}}{x_\beta} \frac{\sin(q r_{\alpha\beta})}{q r_{\alpha\beta}} \exp(-\sigma^2_{\alpha\beta} q^2/2) \tag{10}$$

which represent the partial contributions of a Gaussian distribution of $N_{\alpha\beta}$ atoms of type β in a spherical shell of radius $r_{\alpha\beta}$ and variance $\sigma_{\alpha\beta}$ around an atom α.

In figure 4 the best fits (full lines) and the residuals (dashed lines) are reported. In table 4 the structural parameters obtained from the fitting procedure are reported.

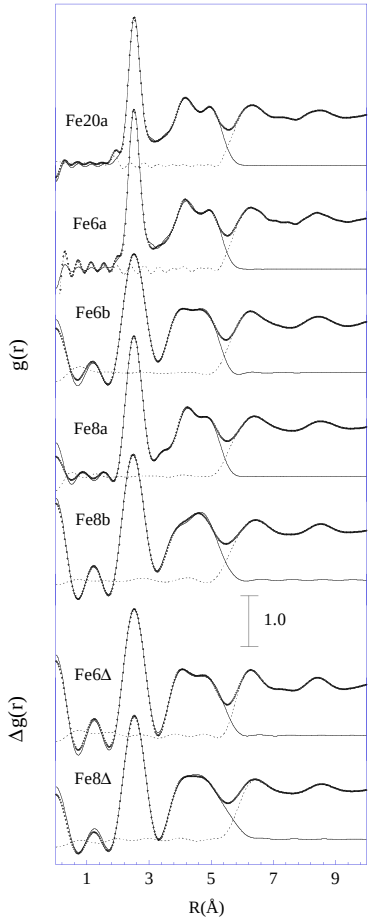

Figure 4. Total and differential pair correlation functions: experimental data (dots), best fits (full line) and residuals (dashed line).

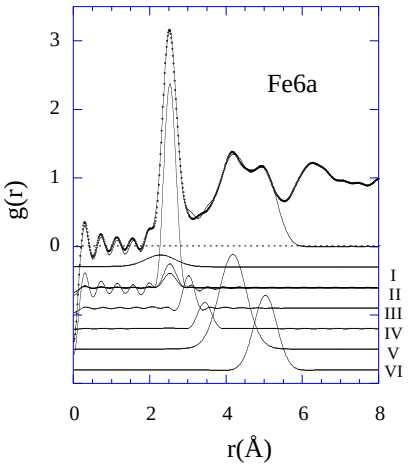

Figure 5. An example of the partial contributions to the total pair correlation functions (sample **Fe6a**). The data (dots) and best fits (full line) are reported together with the partial $g_{\alpha\beta}$-contributions shifted for clarity. The Co–Co, Co–Fe and Fe–Fe partial contributions are reported together at the shell II peak.

5. Results and discussion

Both total and partial pair correlation functions, $g(r)$ and $\Delta g(r)$, present correlations up to 8 Å with features that are typical of metallic glasses: both $g(r)$ and $\Delta g_{\mathrm{Co}}(r)$ (figure 4) present a first intense peak at about 2.5 Å followed by a second one between 4 and 5 Å, with substructures (figure 5) that are more evident in the high-energy data because of their high real-space resolution. In the distant region, the correlations are progressively smoothed out by the disorder but residual oscillations are evident up to (and above) 8 Å, showing that non-negligible medium- and long-range order is still present in these materials. All of these features can be roughly accounted for by the three-dimensional packing of spheres and in fact they are well reproduced by the DRPHS model [3].

Qualitatively, the total and differential pair correlation functions have similar shapes,

Table 4. Best-fit results: the coordination distances in **Fe6** and **Fe8** were made the same for the **a**, **b** and **Δ** data sets, as were the coordination numbers in shells I and II (see the text); thus the values are reported only once.

	Fe20	**Fe6**			**Fe8**		
	a	**a**	**b**	**Δ**	**a**	**b**	**Δ**
Shell I							
R (Å)	2.20(5)	2.29(3)		2.29(3)			
$N_{\mathrm{Co-Si}}$	1.4(5)	1.1(3)					
$N_{\mathrm{Co-P}}$				1.3(3)			
Shell II							
R (Å)	2.54(2)	2.54(2)		2.55(2)			
$N_{\mathrm{Co-Co}}$	9.6(5)	9.8(5)		9.6(6)			
$N_{\mathrm{Co-Fe}}$	1.2(3)	0.20(5)		0.30(6)			
$N_{\mathrm{Fe-Fe}}$	3(1)	4.5(9)		3.5(8)			
Shell III							
R (Å)	3.05(5)	3.02(4)		2.97(5)			
A	1.3(3)	1.4(3)	1.8(3)	(<0.2)	1.9(5)	2.4(4)	(<0.2)
Shell IV							
R (Å)	3.44(8)	3.45(6)		3.45(6)			
A	1.0(3)	1.4(4)	1.9(4)	0.5(3)	1.5(5)	1.4(5)	0.5(3)
Shell V							
R (Å)	4.16(5)	4.16(5)		4.20(6)			
A	21(2)	22(3)	24(3)	20(3)	28(3)	33(3)	27(3)
Shell VI							
R (Å)	5.05(8)	5.03(6)		5.00(6)			
A	25(5)	25(5)	21(5)	27(5)	30(5)	35(5)	23(5)

indicating that the structure of the samples is mainly determined by correlation with Co. However, if we look in more detail, we see first that the $g(r)$s for the high-energy data (**Fe20a**, **Fe6a**, **Fe8a**) show an evident splitting of the second main peak (4–5 Å) and the presence of non-negligible contributions in the region between the two principal peaks (3–4 Å). These features are partially masked in the sets of **b** data, due to the lower resolution of the low-energy data. Comparing **b** and **Δ** data, which have equal resolution, we observe that for the sample **Fe6** the separation between the first and second correlation peaks is more accentuated in $\Delta g(r)$, with apparently no contributions in between. This suggests a minor Co contribution in this region. On the other hand, for **Fe8Δ**, the splitting of the second correlation peak (4–5 Å) is less evident than for **Fe6Δ**, showing a lack of medium-range Co correlation in the ED sample. It is also evident that the $S(q)$ and $\Delta S(q)$ data for the electrodeposited sample are less structured than those for SRQ samples. This still suggests a more disordered structure for sample **Fe8**.

In principle, a full data analysis would take into account a large number of partial contributions (ten and six for SRQ and ED samples respectively). Since this is not possible, we have imposed some reasonable constraints; namely:

(i) The preferential coordination of Fe with B and Co with Si or P, previously observed from XANES and EXAFS [7, 9], was explicitly included in the data analysis by excluding the Fe–Si and Co–B pair correlations.

(ii) The three partially independent correlation functions $g_a(r)$, $g_b(r)$ and $\Delta g(r)$ were all fitted together, with the same set of structural parameters. In particular we notice that the

weight factors of Co–Co, Co–Fe and Fe–Fe pairs show large differences between the **a**, **b** and **Δ** data sets (table 3). Thus, forcing $N_{\mathrm{Co-Co}}$, $N_{\mathrm{Co-Fe}}$ and $N_{\mathrm{Fe-Fe}}$ to be the same for the three data sets allows a reliable determination of the chemical composition of shell II.

(iii) Fitting next-neighbour shells (shells III to VI) is rather difficult due to the large number of parameters involved and the high degree of disorder of the sample; thus we used an alternative expression for $S^{th}(q)$ (equations (1) and (10)), replacing the coefficients $w_{\alpha\beta}(q)N_{\alpha\beta}/x_\beta$ by a peak-area parameter A. In this way, both the peak position and its width are reasonably well determined.

(iv) The EXAFS average distances found in references [7, 9] were used as a starting point in the analysis.

An example of partial $g_{\alpha\beta}(r)$ contributions to $g(r)$ is reported in figure 5. Best-fit results are reported in table 4. To reproduce the structure up to 5.3 Å, six shells are required, some of them composed of two or more partial pair contributions.

The first $g(r)$ ($\Delta g(r)$) peak, at about 2.5 Å, was fitted with two different shells. The first takes into account the Co–Si contribution and the second the metal–metal correlations (Co–Co, Co–Fe, Fe–Fe). The Fe–B correlations were neglected in view of the low coefficient expected (table 3). The first shell of Co was found to be composed of one atom of Si around the Co at about 2.3 Å. Only for sample **Fe20**, the one with higher Fe concentration, did we find a lower distance ($R_{\mathrm{Co-Si}} = 2.2$ Å) that could indicate an Fe–B contribution that is not completely negligible. In fact, from the EXAFS we found two B atoms around Fe at 2.15 Å [7, 8].

In the second shell, the metal–metal correlations were found at about 2.55 Å. This peak is in principle composed of three partial contributions: Co–Co, Fe–Fe and Co–Fe and all the three must be included to fit at the same time the **a**, **b** and **Δ** correlation functions of both samples **Fe6** and **Fe8**. For the samples **Fe20**, **Fe6** and **Fe8**, the total coordination numbers $N_{\mathrm{Co}} = N_{\mathrm{Co-Co}} + N_{\mathrm{Co-Fe}}$ are 10.8, 10 and 9.9 respectively, while the numbers $N_{\mathrm{Fe}} = N_{\mathrm{Fe-Fe}} + N_{\mathrm{Fe-Co}}$ are 7.8, 7.6 and 7, in good agreement with previous EXAFS results.

In a random distribution of metal–metal first neighbours, the expected $N_{\mathrm{M-M}}$ coordination number would be proportional to the total coordination number $N_{i-j}^{RD} \sim N_i x'_j$ with $x'_j = x_j/(x_{\mathrm{Fe}} + x_{\mathrm{Co}})$. We found that the experimental $N_{\mathrm{Fe-Fe}}$ and $N_{\mathrm{Co-Co}}$ are systematically higher than those expected for a random pair distribution (particularly for Fe–Fe correlations), $N_{\mathrm{Fe-Fe}}$ being 3, 4–5 and 3–4 instead of 1.6, 0.5 and 0.6 and $N_{\mathrm{Co-Co}}$ being 9.6, 9.8 and 9.6 instead of 8.6, 9.4 and 9 for samples **Fe20**, **Fe6** and **Fe8**. In contrast, the numbers $N_{\mathrm{Co-Fe}} = 1.2$, 0.2 and 0.3 are always smaller than the expected values of $N_{\mathrm{Co-Fe}}^{RD}$ of 2.1, 0.6 and 0.3 for samples **Fe20**, **Fe6** and **Fe8**. This indicates a preference for homo-atomic correlations over a random metal–metal pair distribution. Moreover, the large number of Fe–Fe correlations suggests a Fe-rich phase separation leaving a Fe-depleted Fe–Co phase. Such chemical ordering, already suggested on the basis of EXAFS data, has been unambiguously evidenced and quantified in the present investigation, mainly thanks to the large differences in the weight factors of the Co–Co, Co–Fe and Fe–Fe phases and their energy dependence (table 3), which allowed us to distinguish between the partial contributions.

The next-neighbour distribution includes four shells at about 3, 3.5, 4.2 and 5 Å. We note that the peak positions are weakly influenced by the sample composition (**Fe6**, **Fe20**) and by the preparation method (**Fe6** and **Fe8**); larger differences can be found in the peak area. First, we focus our attention on the region between the two principal correlation peaks at 3 and 3.5 Å (shells III and IV). These peaks are clearly evident in the high-energy data sets (figure 5) and must be included in the analysis of the low-energy data sets to obtain consistent values of coordination numbers and distances in shells II and V. Shells III and IV present the largest differential effect, i.e. the third shell disappears in both **Fe8Δ** and **Fe6Δ** while the

area of the fourth shell is drastically reduced (table 4). XRS and DAS results indicate a minor Co contribution in this region and support the earlier EXAFS observations that found two Fe–metal shells at 3 and 3.5 Å respectively; thus EXAFS and XRD results suggest an Fe-rich phase separation.

For all of the samples, the second principal peak of the correlation functions is fitted using two shells (V and VI in table 4): the former at about 4.2 Å and the latter at 5 Å. The peak area changes widely among the three data sets; unfortunately the complex nature of the atomic correlations hinders a detailed chemical analysis in that region.

6. Conclusions

Fe–Co-based metallic glasses have been studied by means of XRS and DAS with a view to revealing their atomic structure at short- and medium-range scales. The principal structural features up to about 5 Å have been evidenced and interpreted in terms of structural and chemical order parameters.

We have clearly demonstrated that the Co-rich amorphous alloys present a general tendency toward chemical ordering, showing homo-atomic correlations to be preferred over the random distribution. The chemical ordering is particularly evident for Fe–Fe correlations and indicates the presence of an Fe-rich phase. The existence of a chemically ordered Fe-rich phase already present in the amorphous state should play a central role in the thermodynamics of these materials, providing the nucleation centres for the crystallization process.

Acknowledgments

We are grateful to F D'Acapito, F Colonna and S Pascarelli for help with the beamline set-up. The GILDA project is financed by the Italian institutions CNR, INFM, INFN.

References

[1] Luborsky F E 1980 *Ferromagnetic Materials* ed E P Wohlfarth (Amsterdam: North-Holland)
[2] Polk D E 1972 *Acta Metall.* **20** 485
[3] Finney J L 1977 *Nature* **266** 309
[4] Sadoc J F and Dixmier J 1976 *Mater. Sci. Eng.* **23** 187
[5] De Crescenzi M, Balzarotti A, Comin F, Incoccia L, Mobilio S and Motta N 1981 *Solid State Commun.* **37** 921
[6] García-Arribas A, Fdez-Gubieda M L, Orue I, Barandiarán J M, Herreros J and Plazaola F 1995 *Phys. Rev.* B **52** 12 805
[7] Fdez-Gubieda M L, Orue I, F Plazaola F and Barandiarán J M 1996 *Phys. Rev.* B **53** 620
[8] Orue I, Fdez-Gubieda M L, Plazaola F and Barandiarán J M 1998 *J. Phys.: Condens. Matter* **10** 3807
[9] Fdez-Gubieda M L, García-Arribas A, Orue I, Plazaola F and Barandiarán J M 1997 *Europhys. Lett.* **40** 43
[10] Voropaeva L, Gurov A, Stelmukh V, Novokhatskaya N and Serebryakov A 1995 *J. Non-Cryst. Solids* **192+193** 153
[11] Quintana P, Amano E, Valenzuela R and Irvine J T S 1994 *J. Appl. Phys.* **75** 6940
[12] Serebryakov A, Stelmukh V, Gurov A and Novokhatskaya N 1995 *Nanostruct. Mater.* **5** 481
[13] Magini M, Licheri G, Piccaluga G, Pascina G, and Pinna G 1988 *X-Ray Diffraction of Ions in Aqueous Solutions* (Boca Raton, FL: Chemical Rubber Company Press)
[14] Materlik G, Sparks C J and Fischer J 1994 *Resonant Anomalous X-Ray Scattering Theory and Applications* (Amsterdam: Elsevier) and references therein
[15] Suck J B, Raoux D, Chieux P and Riekel C (ed) 1993 *Methods in the Determination of Partial Structure Factors* (Singapore: World Scientific)
[16] Fuoss P H, Eisenberger P, Warburton W K and Bienenstock A 1981 *Phys. Rev. Lett.* **46** 1537
[17] Herreros J, Barandiarán J M and García-Arribas A 1996 *J. Non-Cryst. Solids* **201** 102
[18] Pascarelli S, Boscherini F, D'Acapito F, Hrdy J, Meneghini C and Mobilio S 1996 *J. Synchrotron Radiat.* **3** 147

[19] Meneghini C, Balerna A, Boscherini F, Pascarelli S, and Mobilio S 1999 *J. Synchrotron Radiat.* **5** 1258
[20] Suorti P, Lienert U and Schulze C 1996 *Proc. 17th Int. Conf. on X-Ray and Inner Shell Processes (Hamburg)* ed R L Johnson, H Schmidt-Böcking and B F Sonnta (Woodbury, NY: AIP Press)
[21] Palinkas G 1973 *Acta Crystallogr.* A **29** 10
Hajdu F 1971 *Acta Crystallogr.* A **27** 73
[22] *International Tables for Crystallography* 1995 vol C, ed A J C Wilson (Dordrecht: Kluwer)
[23] Sasaki S 1989 *KEK Report* 88-14
[24] Dreier P, Rabe P, Malzfeldt W and Niemann W 1984 *J. Phys. C: Solid State Phys.* **17** 3123